





# Oxidation behavior of a nickel-based single crystal superalloy at 1100 °C under different oxygen concentration

Meng Li<sup>1</sup>, Ping Wang<sup>2</sup>, Yan-Qiu Yang<sup>1</sup>, Yi-Zhe Yang<sup>1</sup>, Hai-Qing Pei<sup>3,\*</sup> , Zhi-Xun Wen<sup>1,\*</sup> , and Zhu-Feng Yue<sup>1,2,3</sup>

<sup>1</sup> School of Mechanics, Civil Engineering and Architecture, Northwestern Polytechnical University, Xi'an 710072, People's Republic of China

<sup>2</sup> School of Aerospace Engineering and Applied Mechanics, Tongji University, Shanghai 200092, People's Republic of China

<sup>3</sup> School of Civil Engineering and Transportation, South China University of Technology, Guangzhou 510640, Guangdong, People's Republic of China

Received: 2 November 2021

Accepted: 5 January 2022

Published online:

17 January 2022

© The Author(s), under exclusive licence to Springer Science+Business Media, LLC, part of Springer Nature 2022

## ABSTRACT

The oxidation behavior of a nickel-based single crystal superalloy at 1100 °C under three different oxygen concentrations (10%/21%/30%) was studied. The results showed that the ambient oxygen concentrations had a significant effect on the oxidation rate and oxide layered structures of the tested alloy. With the increase of oxygen concentration, the oxidation rate of the test alloy increased significantly, and the parabolic oxidation rate constants obtained by fitting had a linear relationship with the oxygen concentrations. At 10% and 21% oxygen concentration, Al<sub>2</sub>O<sub>3</sub> was formed on the sample surfaces with the increase of oxidation time, while at 30% oxygen concentration, a typical three-layer oxide layered structure—outer (Ni, Co)O, middle complex oxides with spinel phase structure, and inner Al<sub>2</sub>O<sub>3</sub>—was formed. In addition, the causes of oxide scale spalling, the influence of oxygen concentrations on different oxide layered structures, and the oxidation mechanism based on ionic diffusion were discussed in detail.

## Introduction

As aero-engine turbine blades are used in harsh and extreme environments such as high temperature and high stress, high requirements are placed on the

performance of blade materials. Nickel-based single crystal superalloys are widely used in aero-engine turbine blades due to their excellent creep and fatigue high-temperature mechanical properties [1–3]. However, compared with their excellent high-temperature mechanical properties, their oxidation resistance is

Handling Editor: P. Nash.

Address correspondence to E-mail: peihaiqing@scut.edu.cn; zxwen@nwpu.edu.cn

not so ideal. At present, high-temperature thermal barrier coating is mainly used to avoid oxidation and corrosion damage of this kind of material [4, 5]. Under the actual service conditions, on the one hand, the thermal barrier coating will crack, and peel off due to thermal shock, thermomechanical fatigue, and local stress overload, so that the turbine blade will lose its protective barrier. On the other hand, due to the complex structural design of turbine blades, such as cavity structure and gas film holes, the protective thermal barrier coating cannot be applied. These factors above will lead to the alloy being directly exposed to high-temperature environment and oxidized, resulting in the degradation of material properties, and then affecting the service life of turbine blades. Therefore, it is necessary to study the oxidation behavior of nickel-based single crystal superalloy.

Nickel-based single crystal superalloys contain more than ten kinds of alloy elements, which will interact with each other. In addition, the actual working conditions in material engineering applications are complex and demanding, so the morphological structure and oxidation mechanism of high-temperature oxidation products are complex. Given the above reasons, many meaningful studies have been carried out on the high-temperature oxidation behavior of nickel-based single crystal superalloy. The main factors affecting the high-temperature oxidation behavior of the alloy are summarized as follows: (1) the content of solid solution elements in the alloy, such as Al, Ti, Ta, W, Nb, Re, etc. [6–10]; (2) surface treatment technology, such as surface roughness, grit-blasting, shot peening, and pre-oxidation [11–15]; (3) oxidation temperature [16, 17]; (4) microstructure of the alloy, such as phases, dendrites, and crystal orientations [18–21]; (5) self-generated stress and external load in the oxide scale [22–24]; (6) oxidation atmosphere environment, such as water vapor, SO<sub>2</sub>, CO<sub>2</sub>, etc. [6, 25–28]. For the atmosphere factors affecting the oxidation behavior of nickel-based single crystal superalloy, the effect of water vapor is mainly to introduce additional H element in the oxidation reaction and promote the formation of vacancies in the oxide scale. On the one hand, this leads to an increase in the diffusion rate of alloy elements, thereby increasing the oxidation rate, and on the other hand, it reduces the adhesion of the oxide scale [25, 26]. The effect of SO<sub>2</sub> is to introduce the corrosive element S and react with the elements in

the alloy to form sulfate, so as to change the oxidation into more serious thermal corrosion [27]. Through literature investigation, we did not find the effect of ambient oxygen concentration on the oxidation behavior of nickel-based single crystal superalloy. In practical service, due to the special turbocharging method and fuel combustion of aero-engine, its internal hot components such as turbine blades will experience atmosphere environment different from normal atmospheric oxygen concentration. Therefore, through the experimental design, this study simulates the experimental environment of three different oxygen concentration atmospheres and explores the high-temperature oxidation behavior of nickel-based single crystal superalloy under certain temperature and different oxygen concentration environments, so as to provide more oxidation data of this kind of materials under special atmospheric conditions.

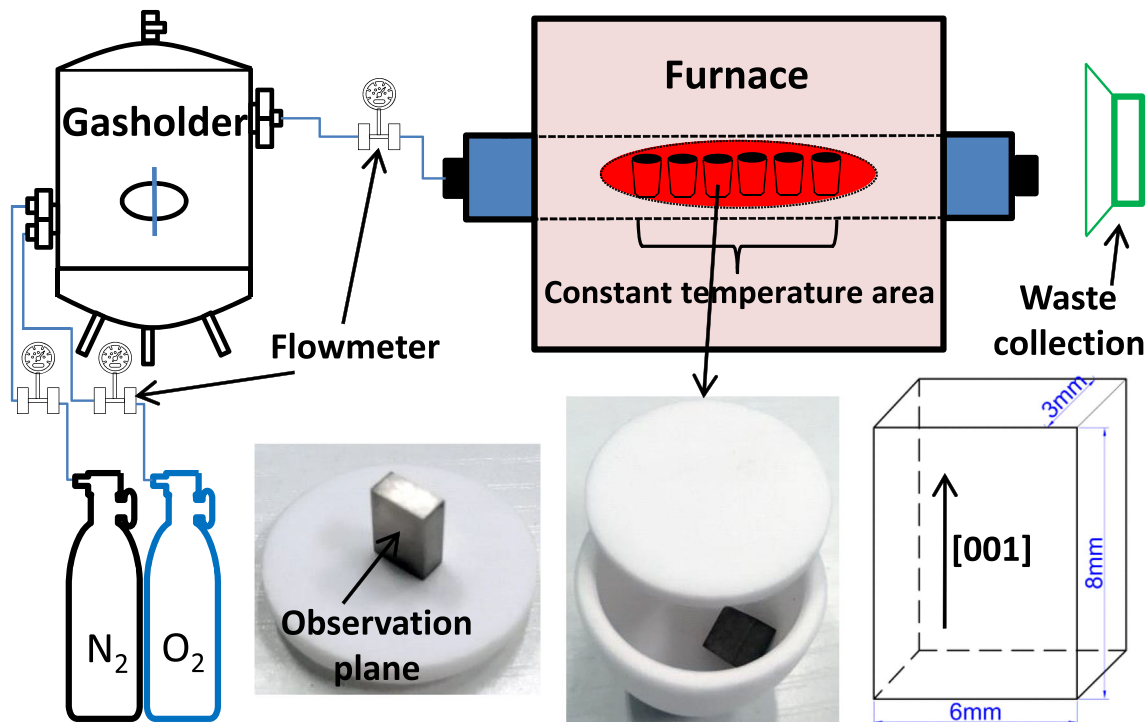
## Materials and experimental method

The material used in this study is a nickel-based single crystal superalloy used in aero-engine turbine blades. The nominal element content is shown in Table 1. First, the master alloy was melted in a vacuum induction melting furnace with pure raw materials, and then a single crystal test bar with [001] orientation was cast in a high-gradient directional solidification vacuum furnace using a spiral crystal selection method. The crystal orientation of the test bar was determined by Laurie's method. The deviation between the [001] crystal orientation of the bar and the stress principal axis was kept within 15 degrees, and the test bar with a deviation within 10 degrees was selected as the experimental material of this study. All experimental materials had undergone heat treatment (1290 °C × 1 h + 1300 °C × 2 h + 1315 °C × 4 h/AC + 1120 °C × 4 h/AC + 870 °C × 32 h/AC (AC: Air cooling)). The oxidation test piece adopted an 8\*6\*3 mm cube sample, the direction of length 8 mm is parallel to the [001] orientation of the material, as shown in the lower-right corner of Fig. 1. All samples surfaces were carefully ground with 1200#SiC sandpaper to ensure the same surface condition. After grinding, all samples were ultrasonically cleaned with acetone (CH<sub>3</sub>COCH<sub>3</sub>) and alcohol (C<sub>2</sub>H<sub>6</sub>O), respectively.

Corundum crucibles with covers were used to hold samples, and all crucibles were repeatedly burned to

**Table 1** Nominal chemical composition of the nickel-based superalloy in wt%

C	Cr	Ni	Co	W	Mo	Al	Ti	Ta	Re	Nb	B	Si	Hf
0.015	4.0	Bal	9.0	8.0	2.0	5.7	≤ 0.10	7.0	2.2	1.0	≤ 0.02	≤ 0.02	1.0

**Figure 1** Schematic diagram of the test process and experimental samples.

constant weight at a temperature 50 °C higher than the experimental temperature before use. During the test, the samples were placed obliquely in the corundum crucible and a certain gap was left between the crucible cover and the crucible so that to ensure the sample was in only point contact with the crucible and fully exposed to the test atmosphere. The test equipment adopted a customized high-temperature vacuum tube furnace equipped with a 2-way gas mixing device, and the temperature control accuracy of the vacuum high-temperature tube furnace is  $\pm 5$  °C. The gas mixing device used mass flow meters to control the gas flow, and the flow error is less than 1%. The experiment creates different oxygen concentration environment by mixing high-purity nitrogen ( $\geq 99.999\%$ ) and high-purity oxygen ( $\geq 99.999\%$ ). Before the test, the tubular furnace was vacuumized, and then the premixed gas was introduced into the reaction chamber at a flow rate of 0.1 L/min. During the test, the mixed gas in the reaction chamber was filled and discharged at the same time to maintain a constant atmosphere environment.

Three different oxygen concentration atmospheres (10% (oxygen deficient), 21% (simulated atmosphere), and 30% (oxygen enriched)) were set up. According to the operating temperature range of aero-engine turbine blades, the experimental temperature was set to 1100 °C. The oxidation time was set as 10 h, 50 h, 100 h, 200 h, 350 h, and 500 h. In engineering practice, the turbine blade surface is mostly parallel to the [001] orientation of the material, so this surface was taken as the main observation plane of this study, that was, the 6\*8 mm plane of the cube sample. The schematic diagram of the test process is shown in Fig. 1.

A precision electronic balance (OHAUS PX85ZH) with an accuracy of 0.0001 g was used to measure the oxidation weight gain of samples by the discontinuous weight gain method (including the mass of exfoliated oxide scale). Ultra-depth of field optical microscope (OM) (VHX-6000) and high-resolution scanning electron microscope (SEM) (ZEISS Gemini300) was used to observe the oxide morphology on the surface and the oxides layered structure on the

cross-section. Energy dispersive spectroscopy (EDS) and X-ray diffraction (XRD) (BRUKER D8 DISCOVER A25) were used to detect the chemical composition and phase composition of oxides.

## Results analysis

### XRD analysis

The samples oxidized for 10 h, 100 h, and 350 h under three oxygen concentrations were selected for XRD test, so as to identify the phase of oxidation products of the test alloy. The phase was calibrated according to the position and intensity of the detected diffraction peak compared with the standard phase. The detection results are shown in Fig. 2. The types of oxides obtained by analysis were as follows: a:  $\text{Al}_2\text{O}_3$ , b:  $(\text{Ni}, \text{Co})\text{O}$ , c:  $\text{TaO}_2/\text{NiTa}_2\text{O}_6$ , d:  $\text{Co}_3\text{O}_4/\text{CoWO}_4/\text{CoCo}_2\text{O}_4$ , e:  $\text{Cr}_2\text{O}_3/\text{NiCr}_2\text{O}_4$ , f:  $\text{NiAl}_2\text{O}_4/\text{CoAl}_2\text{O}_4$ , and g: Matrix. Under the condition of 10% oxygen concentration, the oxides detected at the initial stage of oxidation were mainly simple oxides such as  $(\text{Ni}, \text{Co})\text{O}$ ,  $\text{Al}_2\text{O}_3$ ,  $\text{TaO}_2$ ,  $\text{Co}_3\text{O}_4$ , and  $\text{Cr}_2\text{O}_3$ . As the oxidation time further increased from 100 to 350 h, the diffraction peak intensity corresponding to  $(\text{Ni}, \text{Co})\text{O}$  decreased continuously, the diffraction peak intensity corresponding to  $\text{Al}_2\text{O}_3$  increased significantly, and a small number of complex oxides such as  $\text{NiTa}_2\text{O}_6$ ,  $\text{CoWO}_4$ ,  $\text{CoCo}_2\text{O}_4$ , and  $\text{NiCr}_2\text{O}_4$  appeared. Under the condition of 21% oxygen concentration, the type of oxide was obviously more complex. The diffraction patterns corresponding to oxidation for 10 h/100 h/350 h were basically the same. The detected oxide types were  $\text{Al}_2\text{O}_3$ ,  $\text{Co}_3\text{O}_4/\text{CoWO}_4/\text{CoCo}_2\text{O}_4$ ,  $\text{TaO}_2/\text{NiTa}_2\text{O}_6$ ,  $\text{Cr}_2\text{O}_3/\text{NiCr}_2\text{O}_4$ , and  $\text{CoAl}_2\text{O}_4$ ,  $(\text{Ni}, \text{Co})\text{O}$  according to the decreasing order of diffraction intensity. Under the condition of 30% oxygen concentration, the diffraction pattern was obviously simpler than that of 10% and 21%, and the diffraction peak changes obviously with the increase of oxidation time. The types of oxides detected after oxidation for 10 h were  $(\text{Ni}, \text{Co})\text{O}$ ,  $\text{TaO}_2/\text{NiTa}_2\text{O}_6$ ,  $\text{Al}_2\text{O}_3$ , and the spectral peaks of other oxides could not be observed. After oxidation for 100 h, the diffraction peak became relatively simple, and the detected oxides were mainly  $(\text{Ni}, \text{Co})\text{O}$ . After oxidation for 350 h, the diffraction peaks corresponding to the matrix were very significant, and trace amounts of  $(\text{Ni}, \text{Co})\text{O}$  and  $\text{Al}_2\text{O}_3$  can also be detected.

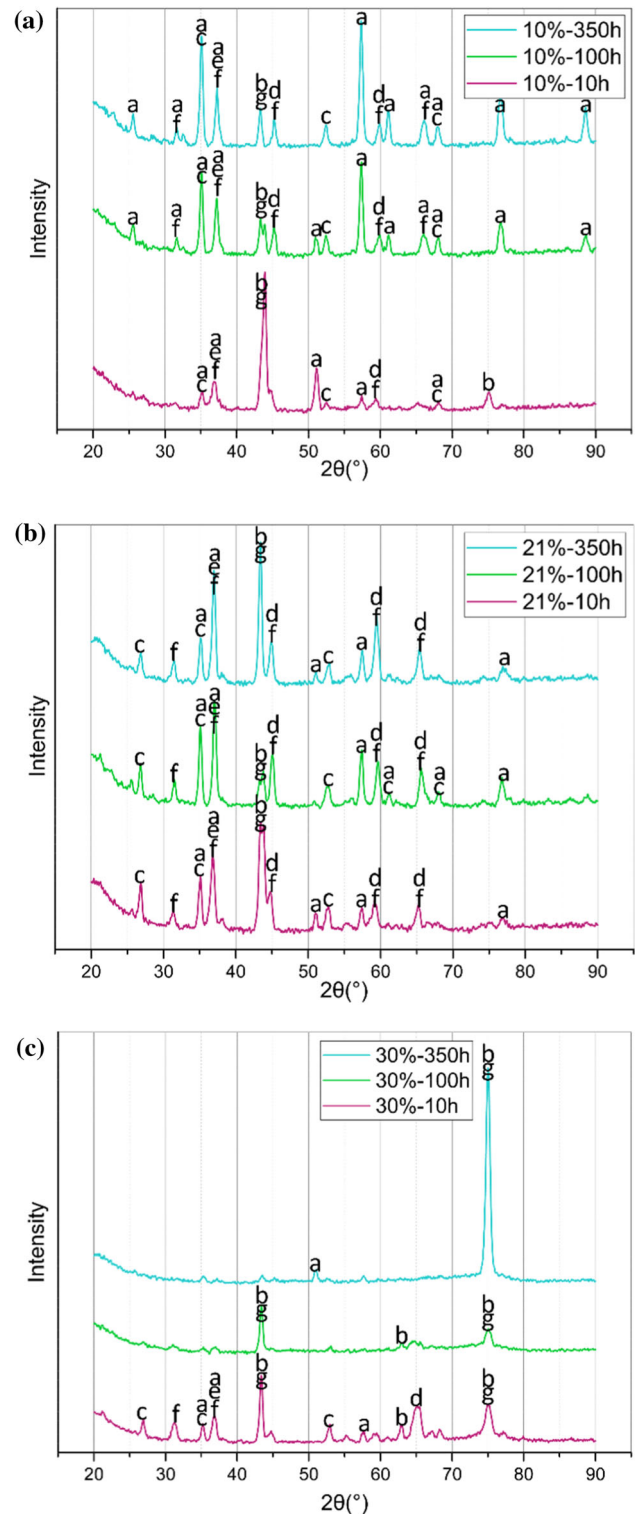


**Figure 2** XRD results of oxides on the surfaces of oxidized samples under 10% (a), 21% (b), and 30% (c) oxygen concentration (a:  $\text{Al}_2\text{O}_3$  b:  $(\text{Ni}, \text{Co})\text{O}$  c:  $\text{NiTa}_2\text{O}_6/\text{TaO}_2$  d:  $\text{CoWO}_4/\text{Co}_3\text{O}_4/\text{CoCo}_2\text{O}_4$  e:  $\text{Cr}_2\text{O}_3/\text{NiCr}_2\text{O}_4$  f:  $\text{NiAl}_2\text{O}_4/\text{CoAl}_2\text{O}_4$  g: Matrix).

### Morphologies analysis of oxides under 10% oxygen concentration

The optical morphology of the sample at different oxidation times under 10% oxygen concentration is shown in Fig. 3a–f. It can be seen that the color of the oxide scale changes from gray to blue, and the oxide scale is relatively complete without serious large area peeling at all oxidation times. It should be noted that after oxidation for 350 h, some small areas of peeling areas with annular characteristics appeared in some areas.

After oxidation for 10 h, a gray oxide scale rich in mixed Ni and Co elements formed on the sample's surfaces. Its composition was 19.05O-8.29Co-72.66Ni (wt%), which was mainly identified as NiO and CoO. Because their stability was similar, the two oxides can form a solid solution single-phase oxide scale, which was labeled as (Ni, Co)O in this paper. The oxide

scale of this layer was in the shape of “pebbles”, loose and porous, and had poor compactness. When the oxidation reached 50 h, there was already a lot of blue  $\text{Al}_2\text{O}_3$  on the surface of the sample, at this time, most of the early generated (Ni, Co)O had been peeled off, and some white dotted complex oxides with spinel phase rich in Cr, Co, Ta, and W would be generated in the gaps of non-peeled loose (Ni, Co)O oxide particles and between (Ni, Co)O and dense  $\text{Al}_2\text{O}_3$  inside, which were mainly  $\text{NiTa}_2\text{O}_4$ ,  $\text{CoWO}_4$ ,  $\text{NiCr}_2\text{O}_4$ , and  $\text{CoCoO}_4$ . Its composition was 20.78O-3.8Al-9.87Cr-7.11Co-18.16Ni-2.16Nb-2Mo-16.48Ta-19.73 W (wt%). In addition, some small areas of peeling areas with annular characteristics appeared in some areas (Figs. 4, 5). The oxide layer structure profile and EDS analysis results after oxidation for 50 h are shown in Fig. 6. After 100 h of oxidation, the external generated blue  $\text{Al}_2\text{O}_3$  further increased, and the outer (Ni, Co)O peeled off more. After 200 h of

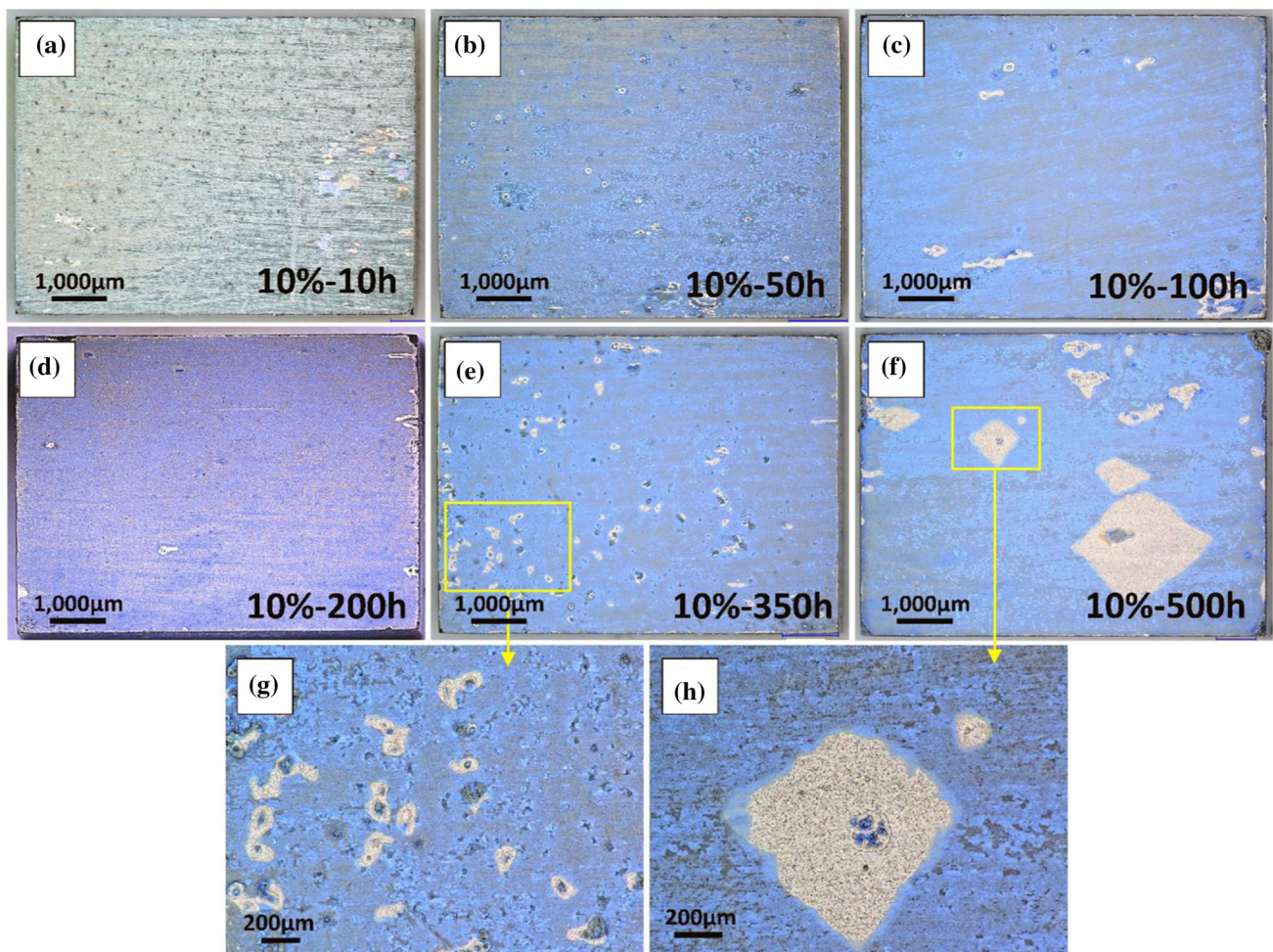


**Figure 3** Optical morphology of samples with different oxidation time at 10% oxygen concentration.

oxidation, the previously generated (Ni, Co)O totally peeled off, and the sample surface was completely covered by blue  $\text{Al}_2\text{O}_3$ . The oxide layer structure profile and EDS analysis results after oxidation for 350 h are shown in Fig. 7. With the further increase of oxidation time, a larger area of spalling area could be observed after reaching 500 h, and some obvious oxide fractures and bright white complex oxides with spinel structure could be observed at the edge of the spalling area. At the same time, the non-peeled outer  $\text{Al}_2\text{O}_3$  was wrinkled under the action of internal stress and produced some microcracks (Fig. 5).

### Morphologies analysis of oxides under 21% oxygen concentration

The optical morphology of oxide scale on the surface of samples with different oxidation time under 21% oxygen concentration is shown in Fig. 8a–f. It could be seen that the surface was mainly blue oxide scale under the condition of oxygen concentration. XRD analysis and EDS elemental analysis showed that it was mainly  $\text{Al}_2\text{O}_3$ . The oxide layer structure profile and EDS analysis results after oxidation for 50 h under 21% oxygen concentration is shown in Fig. 11. With the increase of oxidation time, the peeling area of oxide scale on the surface increased gradually. Since the oxide scale and the peeling area had large color contrast, the changing trend of the proportion of

the oxide scale peeling area with oxidation time could be obtained by statistical analysis of the area of the peeling area through image processing technology, as shown in Fig. 9. It could be seen from the figure that the proportion of oxide scale peeling area basically increased linearly with oxidation time. When oxidized to 350 h, obvious gray-black oxide began to appear in the spalling area, which was identified as (Ni, Co)O. The reason for its formation is that, on the one hand, the surface roughness of the matrix after spallation has increased, and the surface roughness has an important impact on the type of oxidation products [29, 30]. On the other hand, the selective oxidation of Al consumes a large number of Al elements near the surface of the alloy matrix, resulting in a relatively high content of Ni and Co elements, and then oxidation reaction to produce (Ni, Co)O. After oxidation for 500 h, a large amount of gray-black (Ni, Co)O had been generated in the area where the oxide scale peeled off, and a large amount of peeled oxide scale appeared at the bottom of the crucible (Fig. 8g), which was mainly blue  $\text{Al}_2\text{O}_3$  and gray-black (Ni, Co)O.

Since the type of oxide scale on the sample surface did not change significantly with the oxidation time under 21% oxygen concentration, the sample after oxidation for 350 h was selected to carefully observe and analyze the oxides layered structure, as shown in Fig. 10. According to different oxide scale types, the

**Figure 4** Surfaces oxides morphology of samples oxidized for 50 h under 10% oxygen concentration.

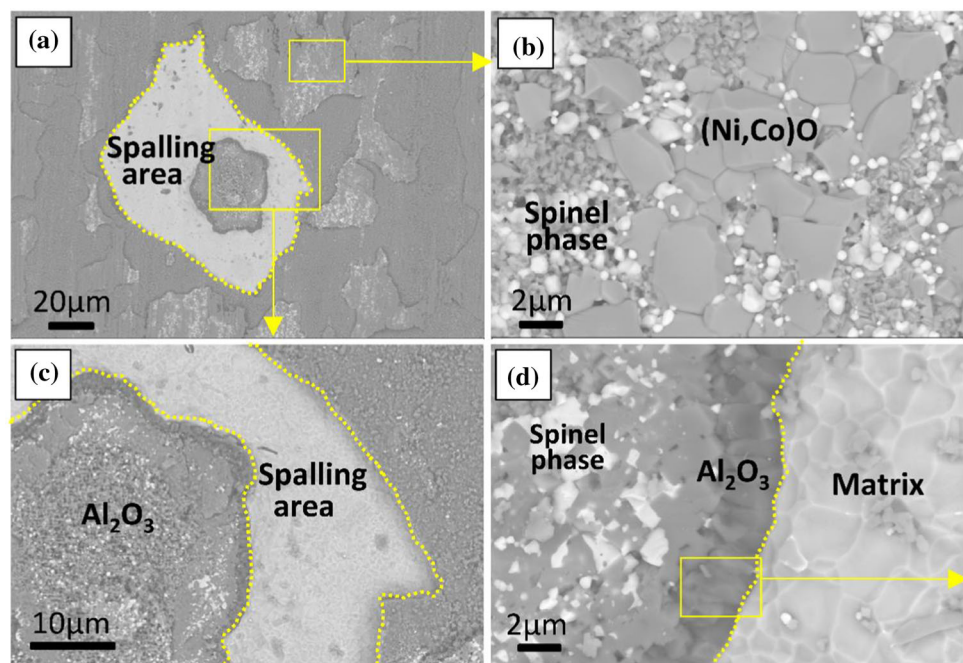


**Figure 5** Surfaces oxides morphology of samples oxidized for 500 h under 10% oxygen concentration.

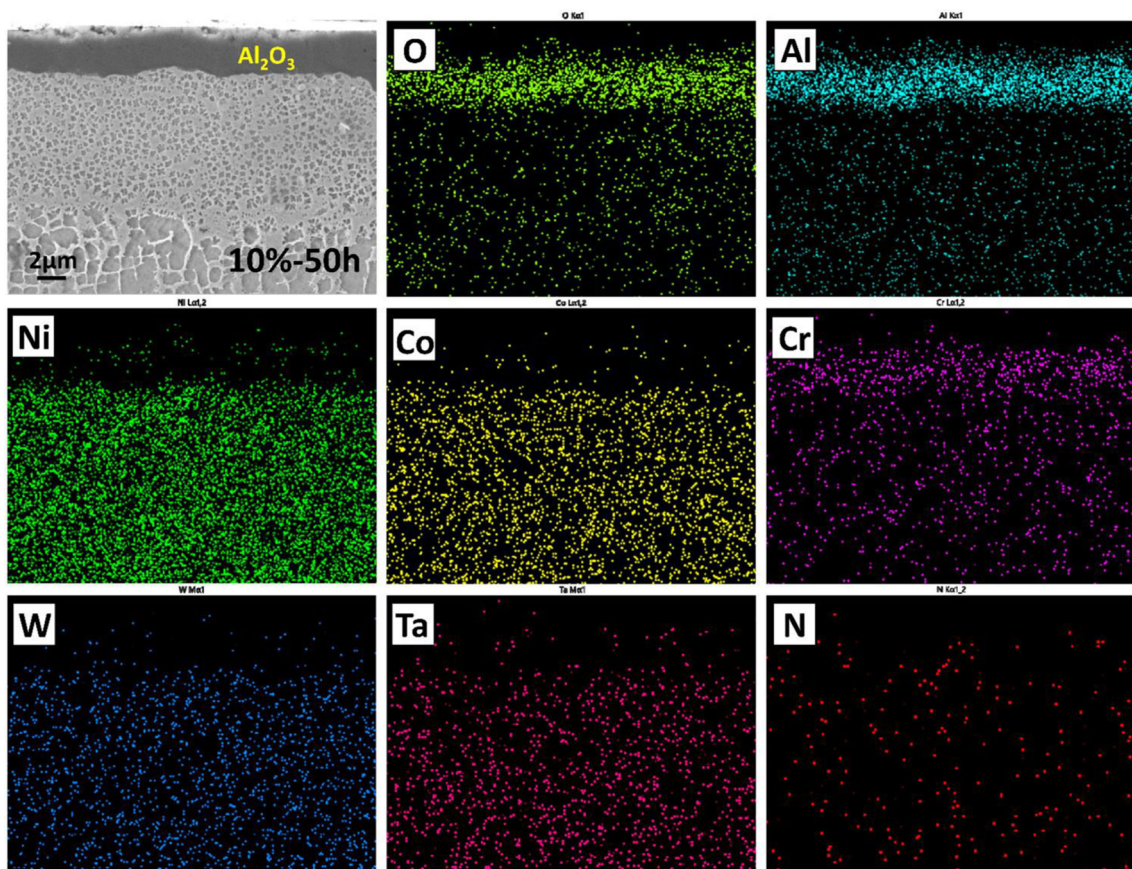
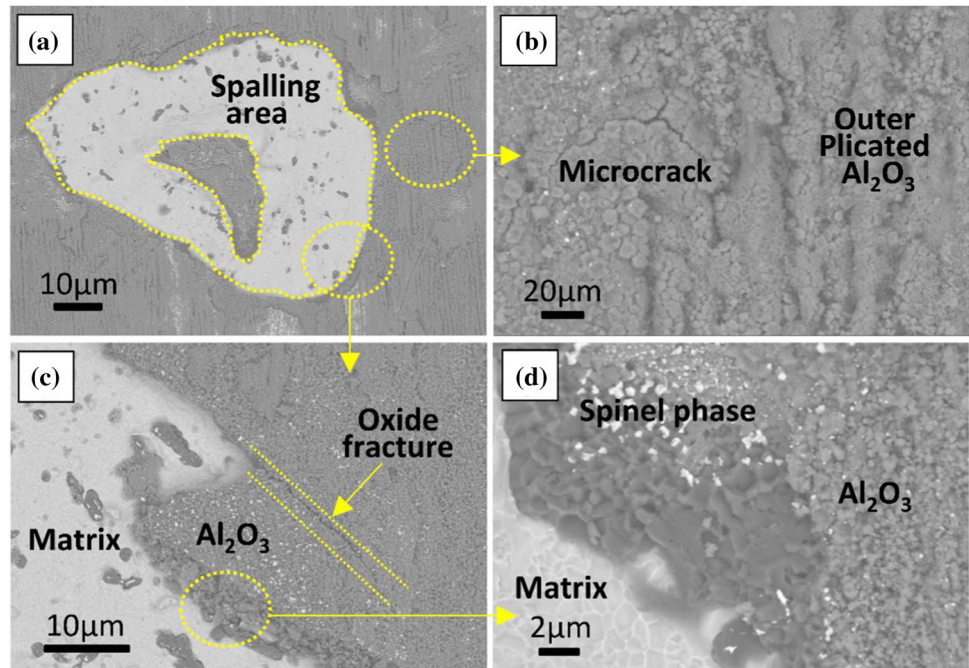


**Figure 6** The oxide layer structure profile and EDS analysis results after oxidation for 50 h under 10% oxygen concentration.

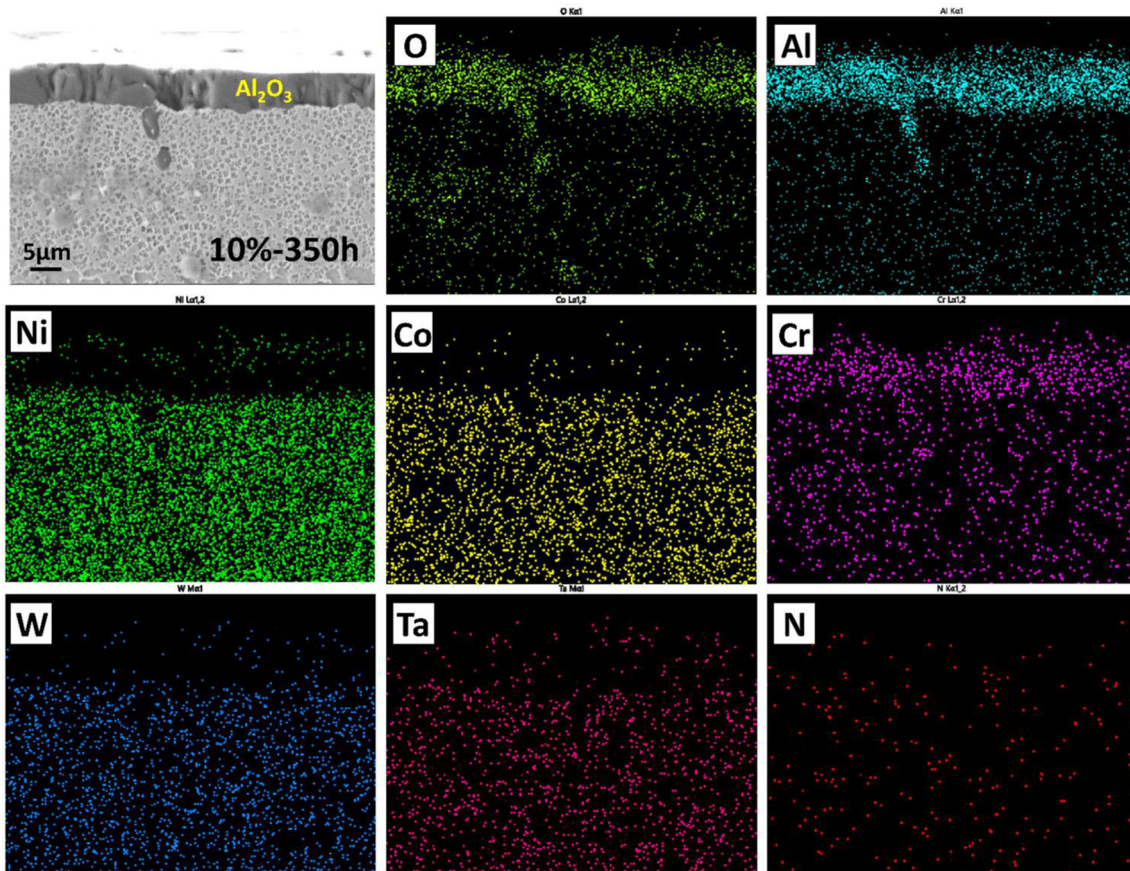


**Figure 7** The oxide layer structure profile and EDS analysis results after oxidation for 350 h under 10% oxygen concentration.

sample surface could be divided into two types of areas, one was the area where blue  $\text{Al}_2\text{O}_3$  was generated in the early stage (Fig. 10b I), and the other was the area where gray-black (Ni, Co)O generated after the early oxide scale peeled off (Fig. 10b II). The micro-morphology of region I is shown in Fig. 10a. It could be seen that the oxide scale here was composed of two layers of  $\text{Al}_2\text{O}_3$ . The external  $\text{Al}_2\text{O}_3$  mixed with various oxides was relatively loose and had peeled off discontinuously, and the internal  $\text{Al}_2\text{O}_3$  was relatively dense (Fig. 11). The profile and elemental composition of this layered structure of double-layer  $\text{Al}_2\text{O}_3$  are shown in Fig. 12. And areas where the oxide layer was completely exfoliated became uneven (Fig. 10c), the surface roughness was significantly increased. The micro-morphology of region II is shown in Fig. 10d ~ i, which was mainly the region where early generated  $\text{Al}_2\text{O}_3$  peeled off, and its formation reason had been explained above. According to the element analysis, the oxide scale of region II could be divided into three layers, the outer layer was pebble-like (Ni, Co)O, the middle layer was

complex oxide rich in W, Cr, Ta, and other elements, and the inner layer was  $\text{Al}_2\text{O}_3$ . Due to poor adhesion, the outermost layer (Ni, Co)O peeled off in many areas. Similarly, such a three-layer structure can also be observed in the cross-sectional view of the sample, its profile and EDS results are shown in Fig. 12. It could be seen that it presented a convex nodule in the cross-sectional direction, and the interface between the oxide scale and the alloy matrix was uneven. In addition, a  $\gamma'$  free layer was observed below the oxide scale, that was, the area where the microstructure of the alloy disappeared or was not obvious. Its composition was 2.04Al-3.5Cr-68.95Ni-8.49Co-2.38Mo-5.8Ta-9.0 W (wt%), which was significantly smaller than the content of Al in the original alloy (5.7%). This was mainly due to the selective oxidation of Al, which constitutes the strengthening phase of the alloy  $\gamma'$  ( $\text{Ni}_3\text{Al}$ ).



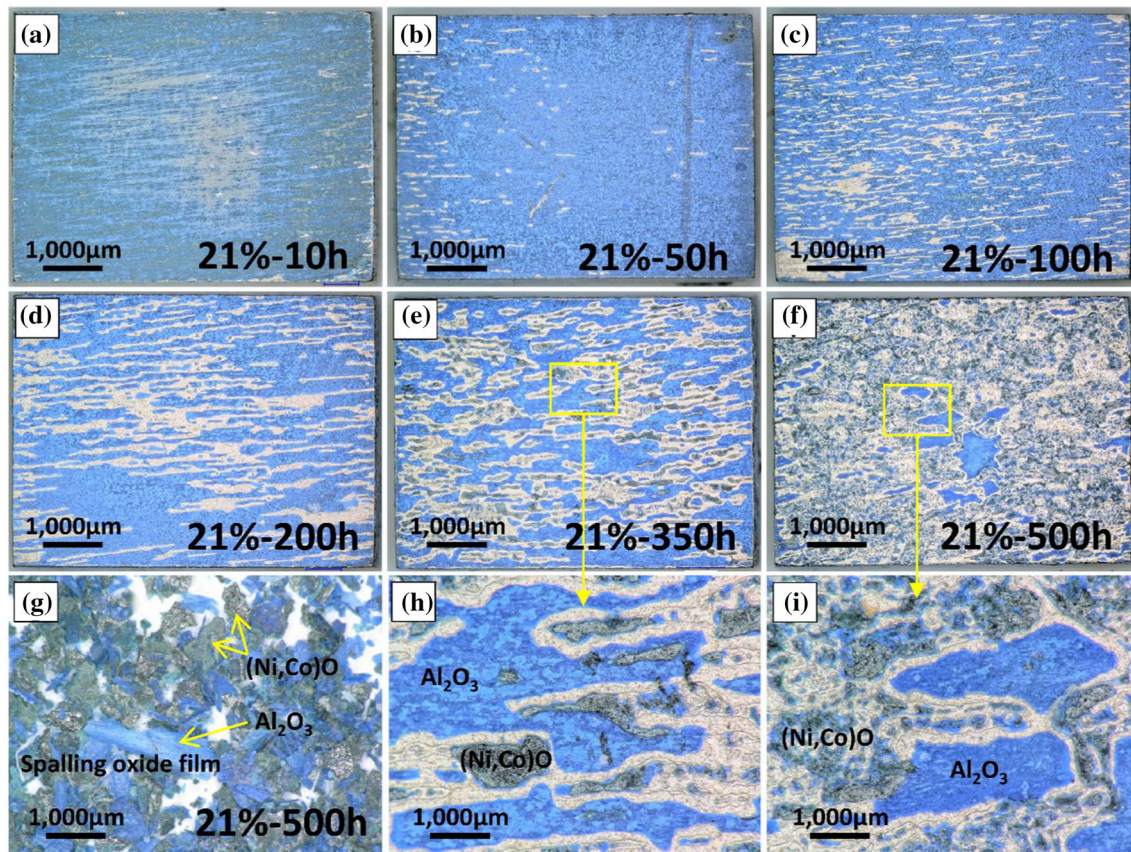


**Figure 8** The optical morphology of oxide scale on the surface of samples with different oxidation time and oxide scale peeled off (500 h) under 21% oxygen.

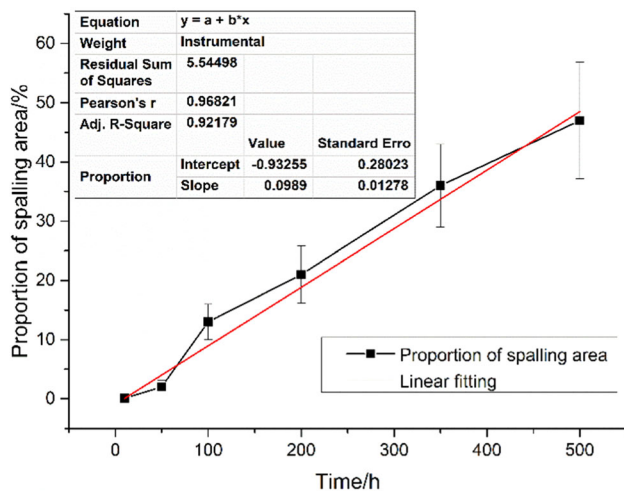


**Figure 9** Statistical diagram of the proportion of oxide scale spalling area on the samples surfaces with oxidation time under 21% oxygen concentration.

### Morphologies analysis of oxides under 30% oxygen concentration

Catastrophic oxidation occurred at 30% oxygen concentration. The structure of the oxide scale was significantly different from that of 10% and 21% and showed the difference between dendrites and interdendrites. After oxidation for 10 h, a layer of gray-black (Ni, Co)O was rapidly formed on the surface. After oxidation for 50 h, the surface of the sample has been completely covered by this oxide scale. After oxidation to 100 h, the oxide scale had peeled off in a large area, and the peeling area presented black stripes parallel to the orientation of alloy [001] (Fig. 13a d). With the progress of oxidation, the oxide scale formed earlier had completely peeled off after oxidation for 350 h, and the sample surface presented obvious black stripes (Fig. 13b e). It could be determined that it grew at the interdendritic of the alloy, which would be explained below. After oxidation for 500 h, a mixed oxide scale of gray-green and blue

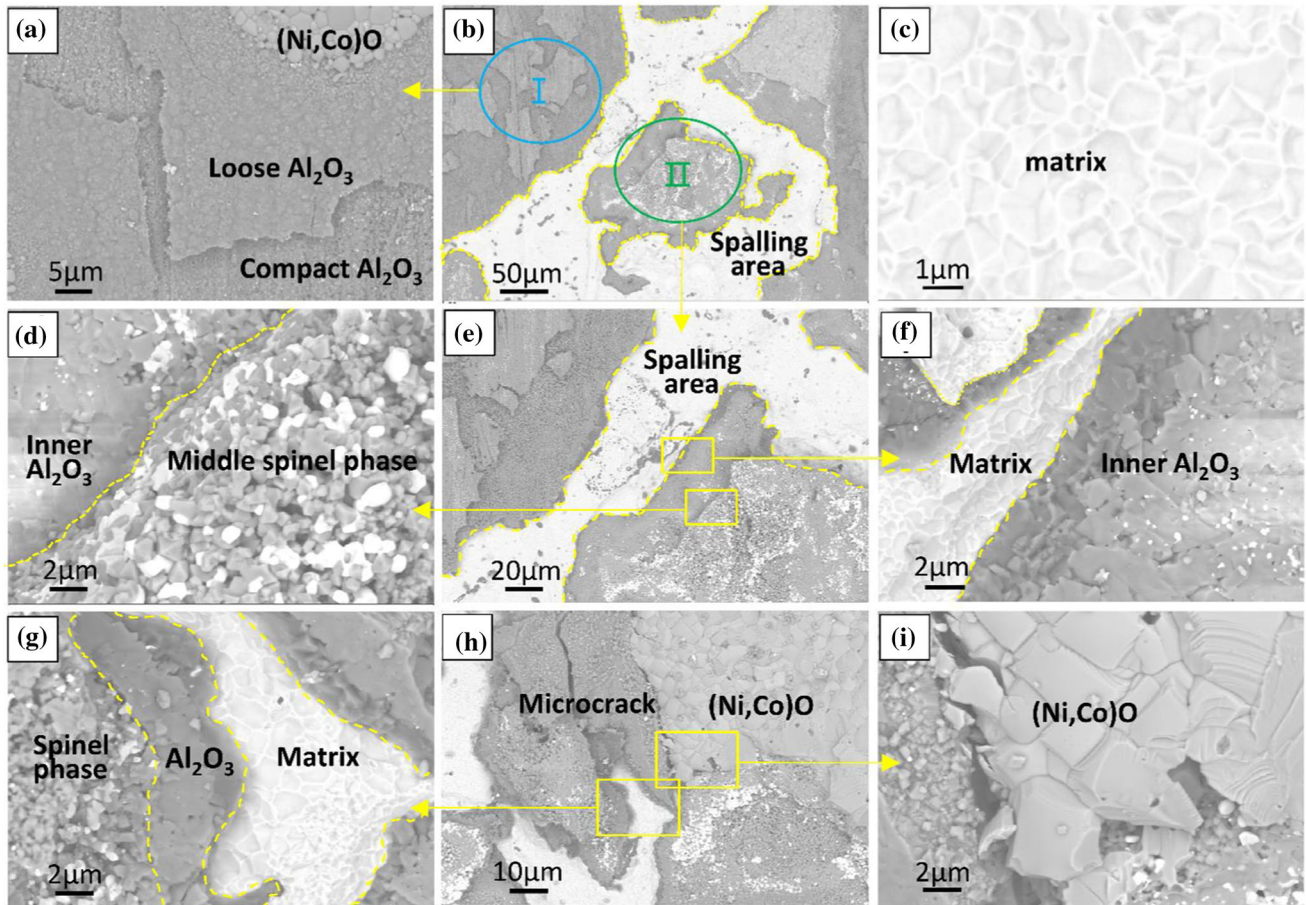


**Figure 10** Surfaces oxides micro-morphology oxidized for 350 h under 21% oxygen concentration.

was regenerated on the sample surface (Fig. 13c f), which was mainly (Ni, Co)O and a small amount of  $\text{Al}_2\text{O}_3$ . At this time, the size of the exfoliated oxide scale collected at the bottom of the crucible (Fig. 13h) was larger than that of the oxide scale exfoliated at the same oxidation time at 21% oxygen concentration. In addition, it could be seen that the edges of the sample were seriously lost under the consumption of oxidation after oxidation for 500 h.

After oxidation for 100 h at 30% oxygen concentration, the surface of the sample was the same oxide layer structure except for the sporadic area of  $\text{Al}_2\text{O}_3$  (Fig. 14a). The same oxide layer structure could be clearly seen from the edges of the peeling and non-peeling areas of the oxide scale, which was mainly divided into three layers, the outer layer was pebble-like (Ni, Co)O, and the middle layer was complex oxide with spinel phase structure rich in W, Cr, Ta, and other elements, and the inner layer was  $\text{Al}_2\text{O}_3$  (Fig. 14b c). This was the same as the layered structure of the raised nodular oxide scale generated in the

peeling area at 21% oxygen concentration (Fig. 12). The oxide scale with such a three-layer structure could also be clearly identified in the sectional view, as shown in Fig. 15, and it can be seen from Fig. 15 that after 100 h of oxidation, the oxide layer in the selected analysis area is separated at the interface between the matrix and the inner alumina layer. And it could be seen from the observation of the optical microscope that black stripes with orientation parallel to alloy [001] were generated in the spalling area of the sample after oxidation at 30% oxygen concentration for 350 h, which was more significant under the electron microscope (Fig. 14e). This phenomenon was mainly due to the dendritic structure formed in the casting process of the test alloy. The Al element of the test alloy would be preferentially segregated between interdendrites during casting solidification. Under the condition of 30% oxygen concentration, the oxide scale inside was mainly  $\text{Al}_2\text{O}_3$ . Due to the large Al content between interdendrites, more reaction elements could be provided to generate more

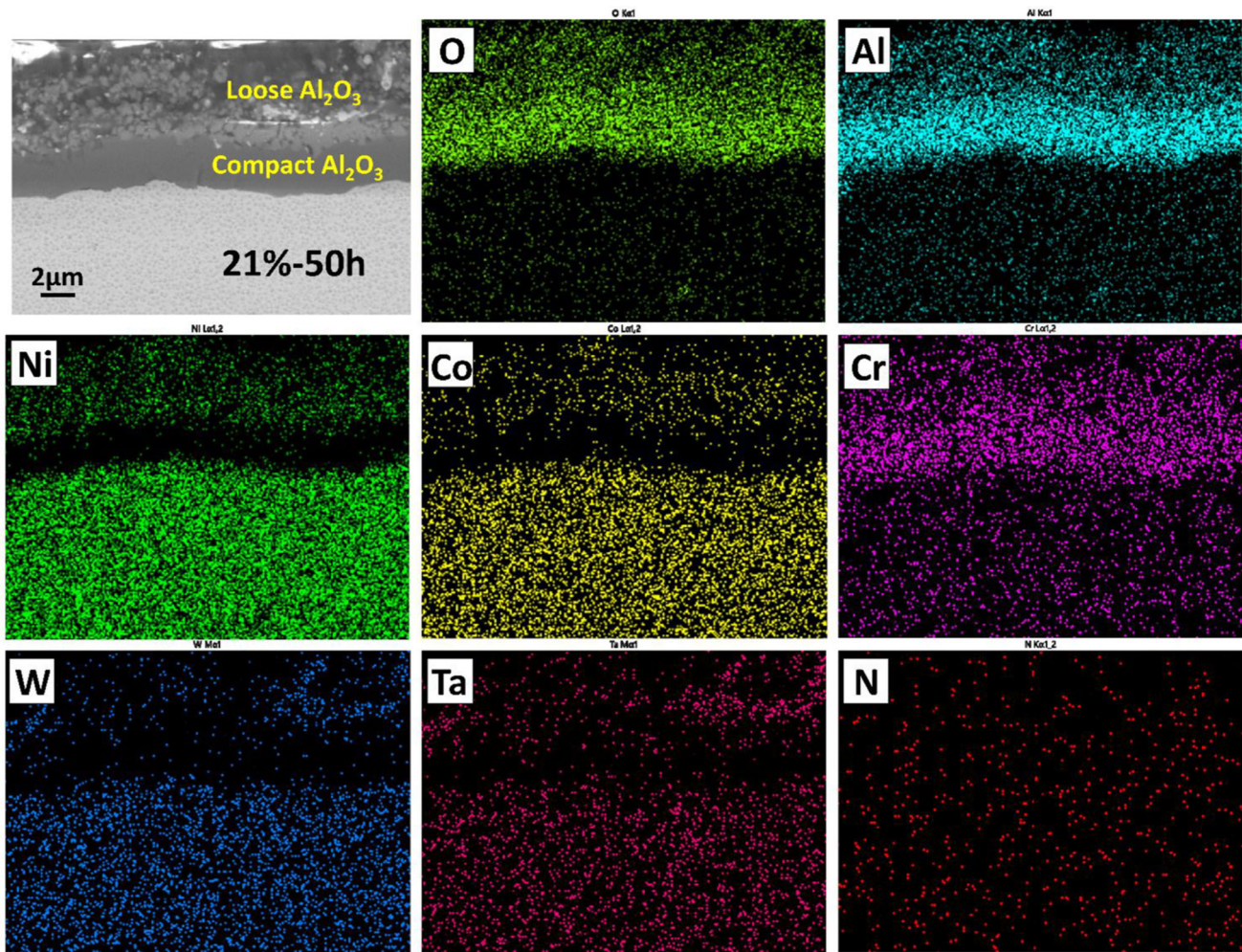


**Figure 11** The oxide layer structure profile and EDS analysis results after oxidation for 50 h under 21% oxygen concentration.

inner  $\text{Al}_2\text{O}_3$ , so as to form  $\text{Al}_2\text{O}_3$  embedded in the matrix of the alloy (Fig. 14d). In addition, at this oxygen concentration, a  $\gamma'$  free layer was formed in the alloy below the oxide scale due to the consumption of Al.

## Discussion

### Oxidation kinetics and characterization

Figure 16a shows the kinetic curve of the oxidation weight gain per unit area of the test alloy with oxidation time at 1100 °C under different oxygen concentrations. It can be seen from the figure that under all oxygen concentration conditions, the oxidation weight gain per unit area increases significantly with the increase of oxidation time, and for the same oxidation time, the oxidation weight gain per unit area

increases significantly with the increase of oxygen concentration. The oxidation weight gain of the test alloy basically conforms to the parabolic law, so the parabolic oxidation rate constant can be fitted by Eq. (1):

$$(\Delta W/A)^2 = k_p t + a \quad (1)$$

where  $\Delta W/A$  is the weight gain per unit area of the sample during oxidation ( $\text{mg}/\text{cm}^2$ ),  $k_p$  is the oxidation rate constant ( $\text{mg}^2 \cdot \text{cm}^{-4} \cdot \text{h}^{-1}$ ),  $t$  is the oxidation time (h), and  $a$  is the constant. The parabolic oxidation rate constant of the test alloy under three oxygen concentrations is shown in the marks in Fig. 16a.

Parabolic coefficient  $k_p$  of the test alloy during oxidation under normal atmospheric conditions can be expressed as:

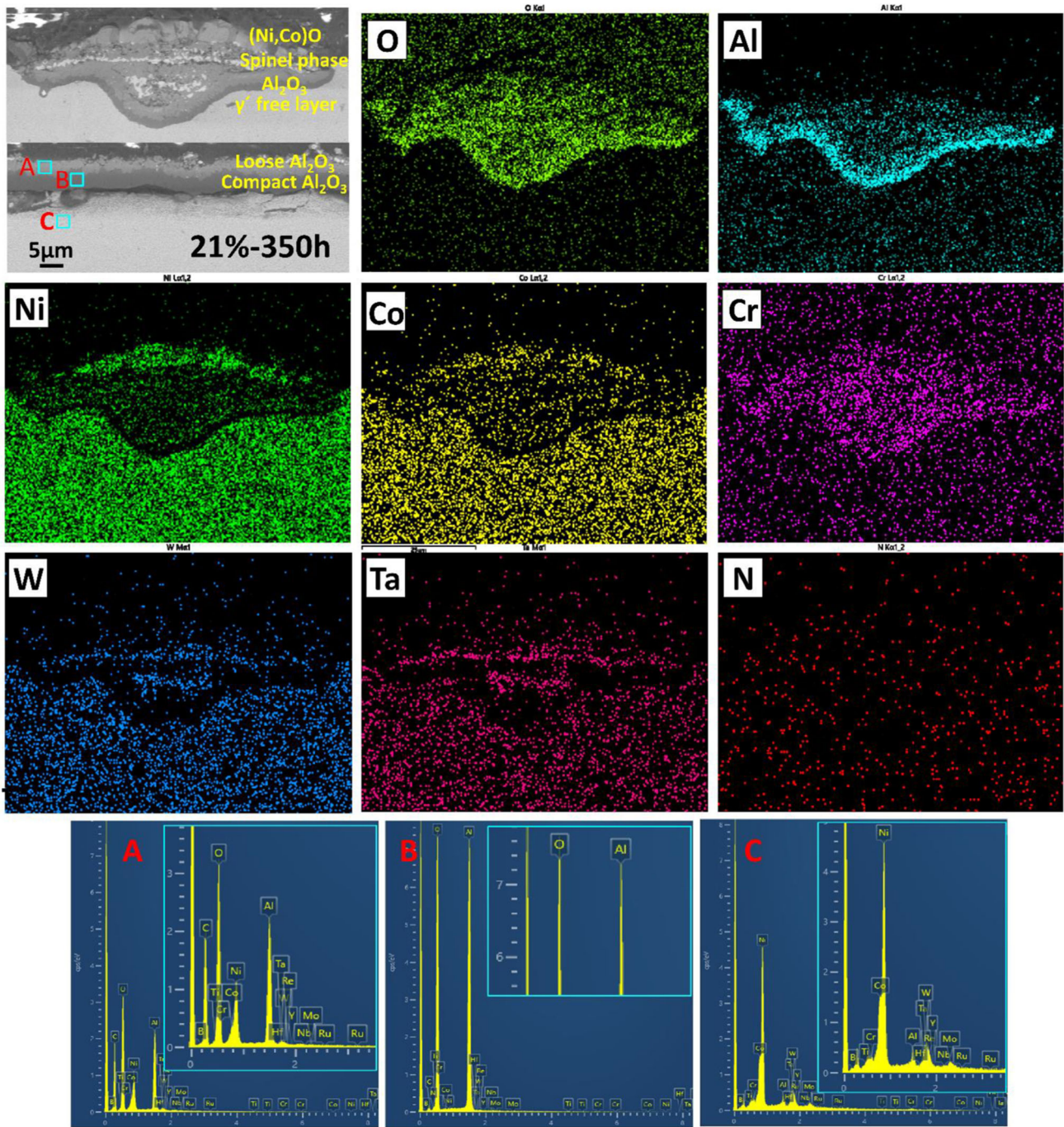


**Figure 12** The oxide layer structure profile and EDS analysis results after oxidation for 350 h under 21% oxygen concentration.

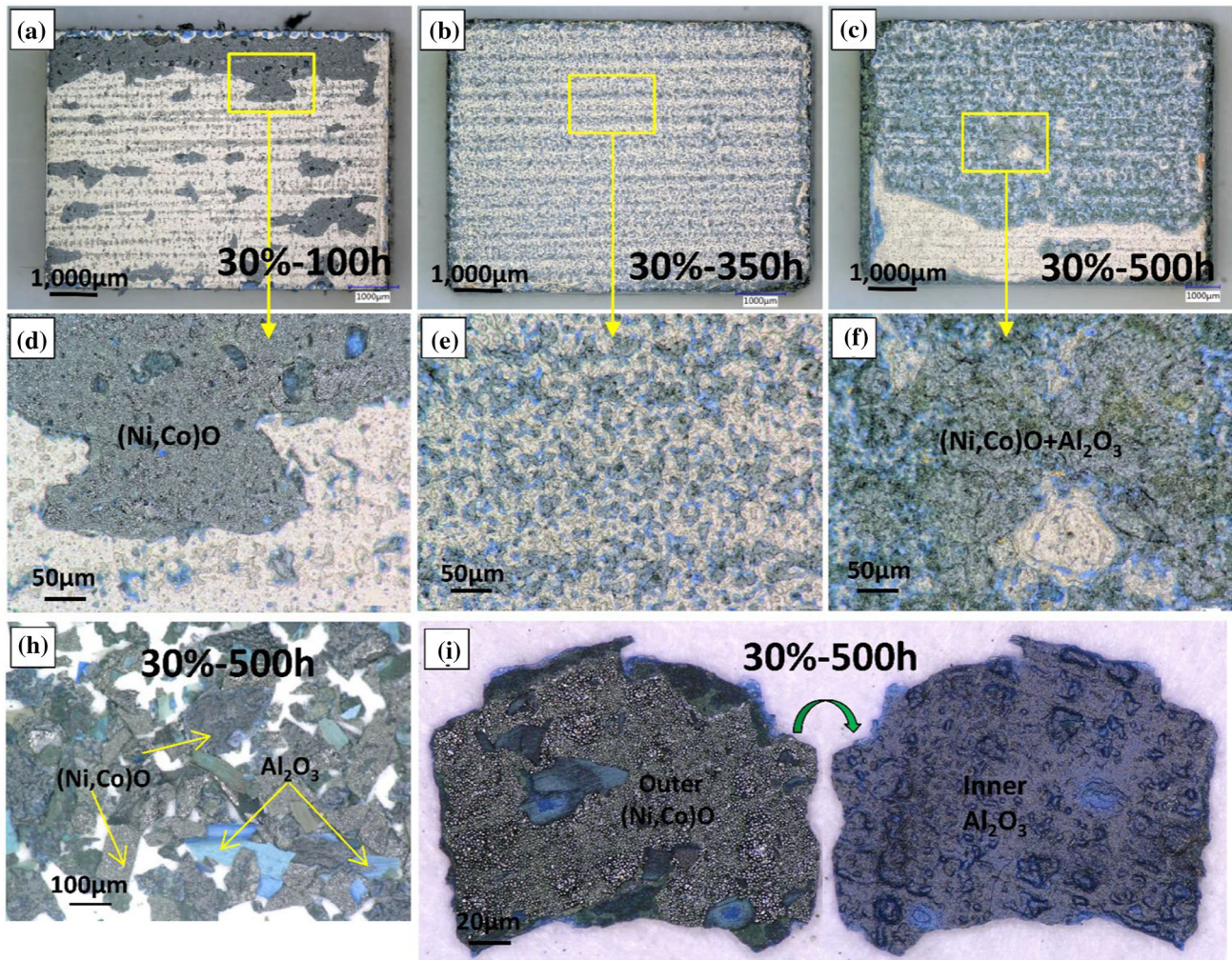
$$k_p = K_0 \exp\left(-\frac{Q}{RT}\right) \quad (2)$$

Figure 16b shows that there is a linear relationship between oxygen concentration and  $\ln k_p$ . With the increase of oxygen concentration, the oxidation rate constant of the test alloy increases significantly.

Therefore,  $k_p$  considering the influence of oxygen concentration is as follows:

$$k_p = K_0 \exp\left(-\frac{Q}{RT}\right) \exp(C\alpha) \quad (3)$$

Among  $\alpha$  is the oxygen concentration, and  $C$  is the correlation coefficient of oxygen concentration. The



**Figure 13** The optical morphology of oxide scale on the surface of samples with different oxidation time and oxide scale peeled off (500 h) under 30% oxygen.

value of  $C$  can be obtained by linear fitting, as shown in Fig. 16b.

### Reasons for spallation of oxide scale

It can be seen from the test results that the peel peeling phenomenon occurred in the samples under the three oxygen concentrations, and the peeling degree increases significantly with the increase of oxygen concentration. The peeling of oxide scale is caused by many factors. It mainly includes the following aspects:

Firstly, the thermal expansion coefficients are different between oxide scale and alloy matrix. For example, the thermal expansion coefficients of NiO,  $\text{Al}_2\text{O}_3$ , and alloy matrix are 17.1, 8.7, and  $15.76 \times 10^{-6} \text{ K}^{-1}$ , respectively [31]. In this study, in

order to accurately control the oxidation time, the samples were put into and taken out of the reaction chamber at high temperature. After the sample was taken out at high temperature, the larger temperature gradient in the process of air cooling would lead to greater thermal stress, which would lead to the peeling of oxide scale. Secondly, it is due to oxide scale growth stress. The oxidation process of the test alloy is accompanied by the change of the volume of the whole system. The PBR values of some corresponding oxides NiO, CoO,  $\text{Al}_2\text{O}_3$ , and  $\text{Ta}_2\text{O}_5$  are 1.65, 1.86, 1.28, and 2.5 ( $\text{PBR} = V_{\text{Ox}}/V_{\text{M}}$ ), respectively [32]. The difference of PBR value leads to a certain degree of compressive stress in each oxide scale, which promotes the cracking and spallation of oxide scale. At the same time, the oxide layer analysis shows that with the increase of oxygen concentration,

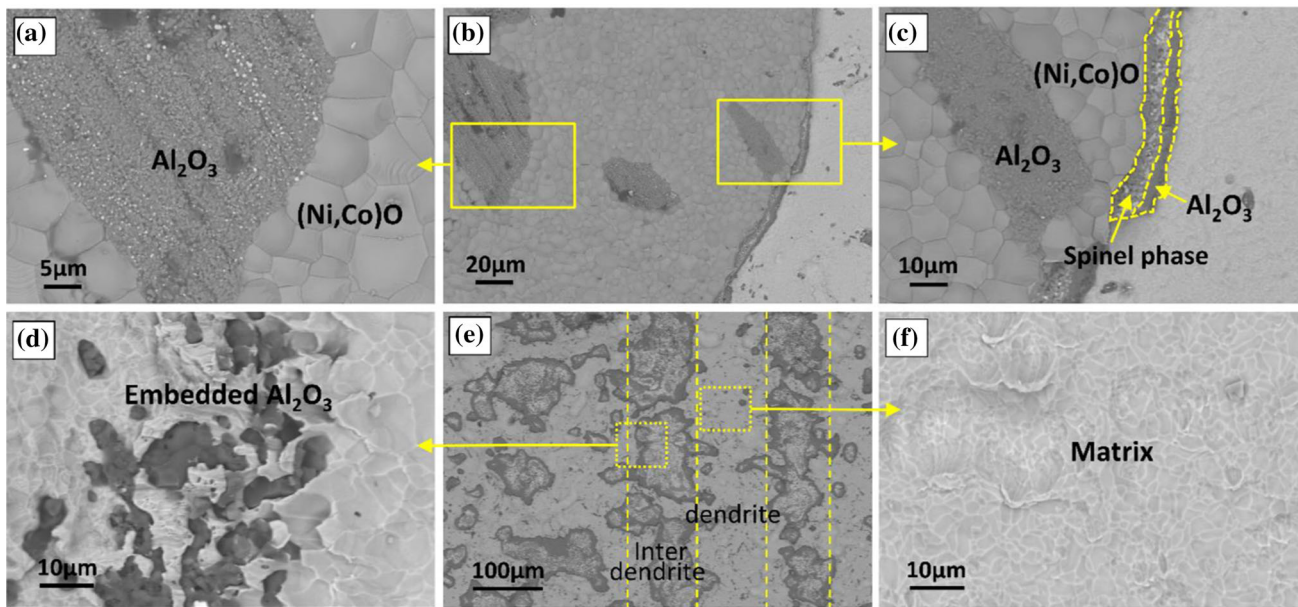


**Figure 14** Surfaces oxides morphology after oxidation for 100 h (a ~ c) and (d ~ f) 350 h under 30% oxygen concentration.

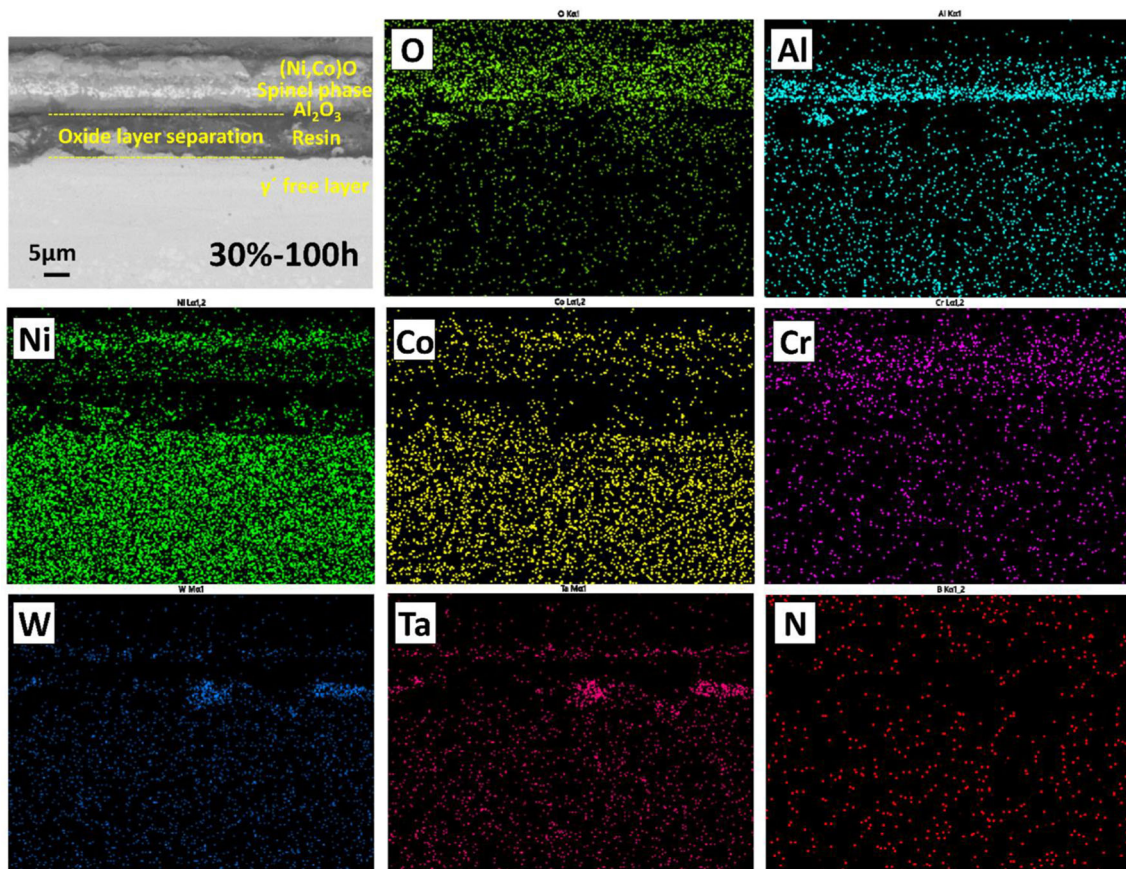


**Figure 15** The oxide layer structure profile and EDS analysis results after oxidation for 100 h under 30% oxygen concentration.

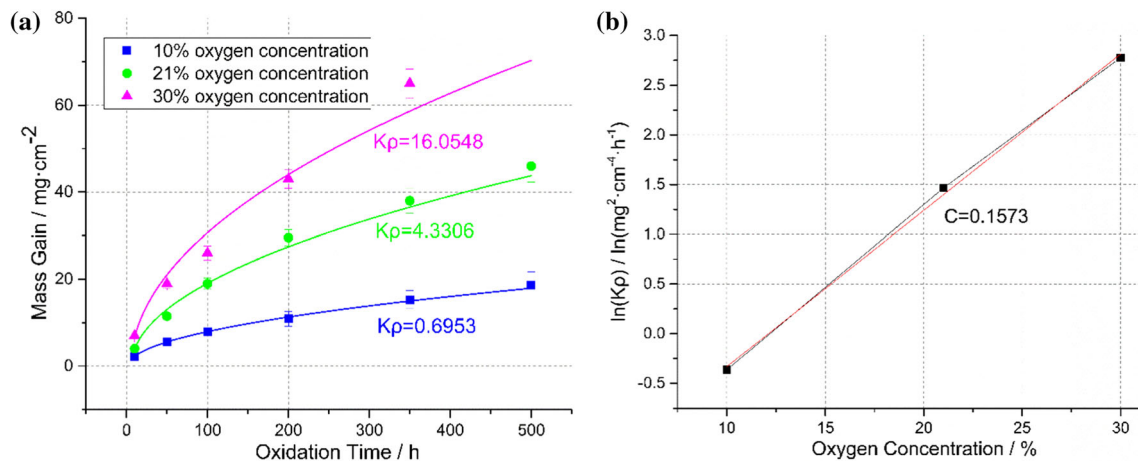


**Figure 16** a Kinetic curves of oxidation weight gain per unit area with oxidation time under different oxygen concentrations and b relationship between oxygen concentrations and oxidation rate constants.

the oxide layer structure becomes more and more complex, from single-layer alumina to double-layer alumina, and then to the typical three-layer oxide layer of this kind of alloy. The complexity of layer structure will also cause more obvious stress mismatch between layers, resulting in single-layer or multi-layer peeling of oxide scale. Therefore, this is one of the reasons why the oxide scale is easier to peel off with the increase of oxygen concentration. In addition, the oxidation kinetics shows that the oxidation rate is greater and thicker oxide layer is formed at higher oxygen concentration, which will cause higher oxide scale growth stress, resulting in more peeling failure of oxide scale at higher oxygen concentration. Finally, it is due to the aggregation of micropores. Under the action of the Kirkendall effect and stress in oxide scale, some micropores will be formed at the interface between oxide scale and alloy matrix, which will reduce the adhesion of oxide scale and promote the spalling of oxide scale [33, 34].

### Effect of oxygen concentration on oxidation progress

According to the test results, the oxygen concentration had a significant effect on the oxidation behavior of the test alloy, mainly in two aspects: oxidation reaction rate and oxides layered structures.

For the oxides layered structures, it could be seen from the previous test results that the oxides layered structure of the test alloy was obviously different under different oxygen concentrations. The oxide on the alloy surface was mainly Al<sub>2</sub>O<sub>3</sub> at 10% and 21%

oxygen concentration, and the oxide on the surface was mainly (Ni, Co)O at 30% oxygen concentration, but the internal oxide scale was Al<sub>2</sub>O<sub>3</sub> under all oxygen concentrations. Therefore, it can be seen that the change of oxides layered structures is closely related to the internal and external oxidation transformation of Al.

The conditions of internal oxidation and external oxidation transition are described by Wagner [35]. In order to form an external Al<sub>2</sub>O<sub>3</sub> layer on a Ni-based alloy, the Al concentration of the alloy needs to exceed a critical value ( $N_{Al}^{(1)}$ ), below which an internal Al<sub>2</sub>O<sub>3</sub> layer will be formed. The value of  $N_{Al}^{(1)}$  can be calculated by Eq. (4) [35]:

$$N_{Al}^{(1)} > \left( \frac{\pi g^*}{\lambda} N_O^{(s)} \frac{D_O V_M}{D_{Al} V_{OX}} \right)^{1/2} \quad (4)$$

where  $N_O^{(s)}$  is the partial pressure of oxygen in the test environment,  $D_O$  and  $D_{Al}$  are the diffusion fluxes of oxygen inward diffusion and solute outward diffusion, respectively,  $V_M$  and  $V_{OX}$  are the molar volumes of the metal and oxide,  $\lambda$  is the valency of the metal in the oxide, and  $g^*$  represents a critical volume fraction of internal alumina precipitates for transition to external scale.

According to formula (4), reduce the internal diffusion flux of oxygen, that is, reduce  $N_O^{(s)}$  (lower oxygen partial pressure), or increase the external diffusion flux  $D_{Al}$  of Al, which will reduce the critical concentration  $N_{Al}^{(1)}$  of Al element required to form Al<sub>2</sub>O<sub>3</sub> external oxide scale. On the contrary,

increasing the internal diffusion flux of oxygen will increase the critical concentration  $N_{Al}^{(1)}$  of Al element required to form  $Al_2O_3$  external oxide scale. During the test, the chemical composition, crystal structure, and test temperature of the sample are the same,  $D_{Al}$  can be considered to be constant, so the main factor affecting the internal and external oxidation of the test alloy will be the oxygen partial pressure  $N_O^{(s)}$  in the test environment. It can be seen from the test results that the oxide on the surface at 10% and 21% oxygen concentration is mainly continuous  $Al_2O_3$ . At this time, the oxygen partial pressure of the experimental environment is low, and the concentration critical concentration required to form the outer  $Al_2O_3$  is low, which is not greater than the maximum diffusion concentration of 5.7% (Al element content of the test alloy) that the test alloy can provide. At 30% oxygen concentration, the oxide on the surface is mainly (Ni, Co)O, at this time, the oxygen partial pressure of the experimental environment is large, and the required concentration critical concentration for the formation of outer  $Al_2O_3$  is greater than 5.7%, so the outer  $Al_2O_3$  cannot be formed.

Despite the higher  $N_{Al}^{(1)}$  can make the alloy form an external  $Al_2O_3$  layer in the initial oxidation stage, but if samples want to continue to generate the external  $Al_2O_3$  layer in the next oxidation stage, the alloy needs to provide enough Al to compensate for the consumption of previous oxidation. The critical concentration of Al in the subsequent oxidation stage can be calculated by Eq. (5) [36]:

$$N_{Al}^{(2)} = \frac{V_m}{32\lambda} \left( \frac{\pi k_p}{D_{Al}} \right)^{1/2} \quad (5)$$

where  $k_p$  is a parabolic oxidation rate constant. From the results of oxidation kinetics,  $k_p$  increases with the increase of oxygen concentration, which leads to the increase of critical concentration  $N_{Al}^{(2)}$ . When it exceeds the maximum concentration that the alloy can provide, the external  $Al_2O_3$  layer cannot be formed. This can also explain why the surface oxide at 30% oxygen concentration is significantly different from the other two lower concentrations.

For the oxidation rate, the analysis of oxidation kinetics shows that the oxidation rate of the test alloy increases significantly with the increase of oxygen concentration. This is directly related to the oxidant content required for chemical reaction. When the

oxygen concentration is high, the  $O^{2-}$  content in the ambient atmosphere is sufficient, which can provide a continuous oxidant source for the oxidation reaction, so as to increase the oxidation rate. In addition, the oxidation rate is also closely related to the type of oxide formed. The protective  $Al_2O_3$  formed on the surface at 10% and 21% oxygen concentration not only has slow growth rate, but also has good adhesion, which can inhibit the diffusion of other reactive elements and reduce the oxidation rate of the alloy [37, 38].

### Oxidation mechanism

The relative charge difference in oxide is the driving force of oxidation and controls the power of oxidation process [39]. According to the main oxidation products of the test alloy, its elements can be divided into two categories: One is Ni, Co, Cr, etc., its oxides belong to metal deficient oxides (P-type), which are mainly formed by the reaction of metal cations diffused outward to the oxide scale/oxidation atmosphere interface with the oxidation atmosphere and grow to the outside of the alloy matrix [40]. The other is Al, W, Ta, etc., their oxides belong to metal surplus type (N-type) oxides, which are mainly generated by the reaction of metal cation with oxygen anion diffusion inward at the oxide scale/matrix interface, and grow toward the alloy matrix [41].

Through the analysis of previous test results, the oxidation mechanism of nickel-based single crystal superalloy under different oxygen concentrations was summarized, and the corresponding schematic diagram is drawn, as shown in Fig. 17.

Under the condition of 10% oxygen concentration, in the initial oxidation stage, oxygen rapidly attached to the surface and reacted with  $Ni^{2+}$  and  $Co^{2+}$  on the alloy surface to form (Ni, Co)O. Oxygen ions passed through the (Ni, Co)O oxide scale and formed internal  $Al_2O_3$  with outward diffused  $Al^{3+}$  in the lower layer. The inward diffused  $O^{2-}$  and outward diffused  $Cr^{3+}$ ,  $W^{6+}$ ,  $Ta^{5+}$  generated  $TaO_2$ ,  $Cr_2O_3$ ,  $WO_3$ , and other oxides at the (Ni, Co)O/ $Al_2O_3$  interface. These oxides would have solid solution reaction with the outermost (Ni, Co)O:  $NiO + Cr_2O_3 = NiCr_2O_4$ ,  $NiO + Ta_2O_5 = NiTa_2O_6$ ,  $CoO + Co_2O_3 = CoCo_2O_4$ ,  $4TaO_2 + O_2 = 2Ta_2O_5$ ,  $CoO + WO_3 = CoWO_4$ , forming some complex oxide particles with spinel phase. In the subsequent oxidation process, the first formed (Ni, Co)O and spinel oxide particles would



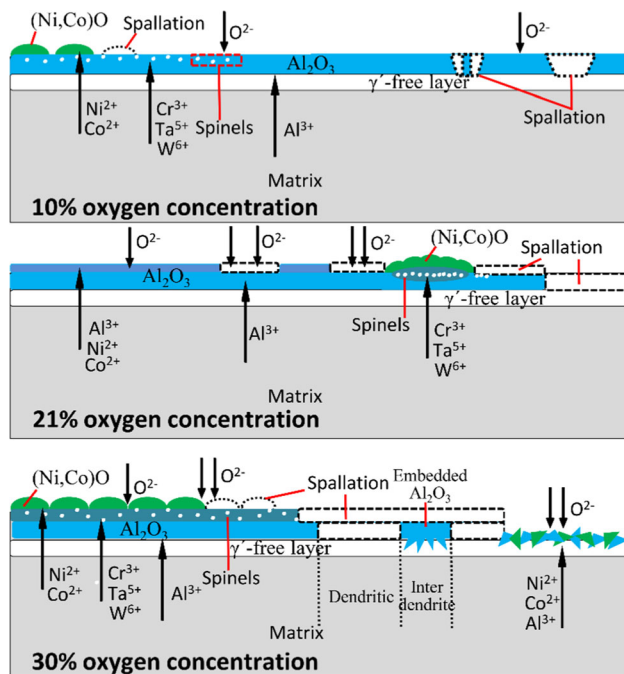


**Figure 17** Schematic diagram of oxidation mechanism of test alloy at three different oxygen concentrations.

peel off rapidly due to looseness and poor adhesion.  $\text{Al}^{3+}$  continuously diffuses outward, gradually generated continuous  $\text{Al}_2\text{O}_3$  on the outer surface, and finally formed a uniform  $\text{Al}_2\text{O}_3$  protective film on the sample surface.

Under the condition of 21% oxygen concentration, the outwardly diffused cations such as  $\text{Al}^{3+}$ ,  $\text{Ni}^{2+}$ ,  $\text{Co}^{2+}$ ,  $\text{Cr}^{3+}$ ,  $\text{W}^{6+}$ , and  $\text{Ta}^{5+}$  reacted with oxygen to quickly form an oxide scale with the main component of  $\text{Al}_2\text{O}_3$  on the sample surface, and then  $\text{O}^{2-}$  passed through the oxide scale and reacted with the outwardly diffused  $\text{Al}^{3+}$  in the alloy/oxide scale interface to form a dense layer of  $\text{Al}_2\text{O}_3$ . In the subsequent oxidation process, the outer layer of the double-layer  $\text{Al}_2\text{O}_3$  oxides layered structure gradually peeled off due to poor adhesion, and only a layer of uniform and dense  $\text{Al}_2\text{O}_3$  was left on the sample surface. In the later stage of oxidation, the dense inner layer  $\text{Al}_2\text{O}_3$  would gradually peel off due to the internal stress of the film too. In the exfoliated area, due to the change of surface state, some nodular oxides with typical three-layer oxides layered structure were generated: the outer layer was  $(\text{Ni}, \text{Co})\text{O}$ , the middle layer was a complex oxide with spinel phase structure rich in  $\text{W}$ ,  $\text{Cr}$ ,  $\text{Ta}$ , and other elements, and the inner layer was  $\text{Al}_2\text{O}_3$ , which was the same as the

oxygenated layer structure at 30% oxygen concentration.

At 30% oxygen concentration,  $\text{Ni}^{2+}$ ,  $\text{Co}^{2+}$  reacted with oxygen to rapidly generate  $(\text{Ni}, \text{Co})\text{O}$  on the surface,  $\text{O}$  diffused inward and selectively oxidized with outwardly diffused  $\text{Al}^{3+}$  at the interface to form  $\text{Al}_2\text{O}_3$ , and then complex oxygenates  $\text{NiTa}_2\text{O}_6$ ,  $\text{CoCo}_2\text{O}_4$ , and  $\text{NiTa}_2\text{O}_6$  with spinel phase were formed by solid solution reaction at the  $(\text{Ni}, \text{Co})\text{O}/\text{Al}_2\text{O}_3$  interface. The formation reason was the same as the initial oxidation stage of 10% oxygen concentration. At this concentration, the oxide scale would peel off quickly, and  $\text{Al}_2\text{O}_3$  embedded in the alloy matrix was formed in the peeling area due to the segregation of  $\text{Al}$  element between interdendrites. In the later oxidation process,  $\text{Al}^{3+}$ ,  $\text{Ni}^{2+}$ , and  $\text{Co}^{2+}$  reacted with oxygen in the peeling area to form a mixed oxide scale composed of  $\text{Al}_2\text{O}_3$  and  $(\text{Ni}, \text{Co})\text{O}$ .

In addition, under the conditions of three kinds of oxygen concentration, a  $\gamma'$  free layer was formed in the matrix below the oxide scale due to the depletion of  $\text{Al}$  element, which was the main component of  $\gamma'$  ( $\text{Ni}_3\text{Al}$ ).

## Conclusions

In this study, the oxidation behavior of a nickel-based single crystal superalloy at 1100 °C under 10% (oxygen deficient), 21% (simulated atmosphere), and 30% (oxygen enriched) three different oxygen concentrations was studied by means of microscope (OM), field emission scanning electron microscope (SEM), X-ray diffraction (XRD), energy dispersive spectrometer (EDS), and customized high-temperature furnace. The main conclusions were as follows:

1. The oxygen concentration had a significant effect on the oxide layered structures of the test alloy. At 10% oxygen concentration, the oxide scale was mainly a layer of uniform and dense  $\text{Al}_2\text{O}_3$ . At 21% oxygen concentration, the oxide scale is mainly a double layer of  $\text{Al}_2\text{O}_3$ . At 30% oxygen concentration, the generated oxides were mainly divided into three layers: outer  $(\text{Ni}, \text{Co})\text{O}$ , middle complex oxide scale with spinel phase rich in  $\text{W}$ ,  $\text{Ta}$ ,  $\text{Cr}$ ,  $\text{Ni}$ ,  $\text{Co}$ , and other elements, and inner  $\text{Al}_2\text{O}_3$ . The increase of oxygen concentration increased the critical concentration  $N_{\text{Al}}$  required

to produce stable external alumina, resulting in the change of oxide layered structures.

2. With the increase of oxygen concentration, not only the oxidation rate increases significantly, but also the oxide scale is easier to peel off. The oxidation kinetics curve basically conformed to the parabolic law, and there was a linear relationship between oxidation rate constant and oxygen concentration at different oxygen concentrations. The higher oxygen concentration provided a continuous oxidant source for the oxidation reaction, which increased the oxidation rate of the test alloy. At higher oxygen concentration, more complex layer structure and higher internal stress mismatch lead to a significant increase in the peeling degree of oxide scale.
3. Based on the diffusion of alloy metal cations and reaction atmosphere anions, a mechanism model of oxidation behavior of nickel-based single crystal superalloy at 1100 °C under different oxygen concentration was proposed.

## Acknowledgements

This research was funded by the National Natural Science Foundation of China (No.: 51875462, 52105147), the Natural Science Basic Research Plan in Shaanxi Province of China (No.: 2020JC-16), the National Science Technology Major Project of China (No.: 2017-IV-0003-0040, 2017-V-0003-0052) and Tai-cang Scientific Research Institute Innovation leading special plan (No.: tc2019dyds11).

## Declarations

**Conflict of interest** The authors declare that they have no known competing financial interests or personal relationships that could have appeared to influence the work reported in this paper.

## References

- [1] Reed RC (2008) The superalloys: fundamentals and applications. Cambridge University Press, London
- [2] Guo J (2008) High-temperature alloy materials. Science Press, Beijing
- [3] Zhang J, Wang L, Wang D et al (2019) Recent progress in research and development of nickel-based single crystal superalloys. *Acta Metall Sin* 55(9):1077–1094. <https://doi.org/10.11900/0412.1961.2019.00122>
- [4] Padture NP, Gell M, Jordan EH (2002) Thermal barrier coatings for gas-turbine engine applications. *Science* 296(5566):280–284. <https://doi.org/10.1126/science.1068609>
- [5] Li Z, Song Y (2021) Thermal barrier coating for aerial and aerospace engine. *Inorgan Organ Thin Films Fundam Fabr Appl* 2:615–645. <https://doi.org/10.1002/9783527344987.ch19>
- [6] Wollgarten K, Galiullin T, Nowak WJ, Quadackers WJ, Naumenko D (2020) Effect of alloying additions and presence of water vapour on short-term air oxidation behaviour of cast Ni-base superalloys. *Corros Sci* 173:108774. <https://doi.org/10.1016/j.corsci.2020.108774>
- [7] Gao S, He B, Zhou L et al (2020) Effects of Ta on the high temperature oxidation behavior of IN617 alloy in air. *Corros Sci* 170:108682. <https://doi.org/10.1016/j.corsci.2020.108682>
- [8] Wang X, Li J, Shi Z, Liu S, Yue X (2017) Effect of W content on oxidation resistance of experimental third generation single crystal superalloys. *Rare Metal Mater Eng* 46(9):2493–2498
- [9] Ye X, Yang B, Nie Y et al (2021) Influence of Nb addition on the oxidation behavior of novel Ni-base superalloy. *Corros Sci* 185:109436. <https://doi.org/10.1016/j.corsci.2021.109436>
- [10] Huang L, Sun XF, Guan HR, Hu ZQ (2006) Effect of rhenium addition on isothermal oxidation behavior of single-crystal Ni-based superalloy. *Surf Coat Technol* 200(24):6863–6870. <https://doi.org/10.1016/j.surfcoat.2005.10.037>
- [11] Zhao Y, Sun F, Jiang P et al (2021) Effects of roughness on stresses in an oxide scale formed on a superalloy substrate. *Coatings* 11(4):479. <https://doi.org/10.3390/coatings11040479>
- [12] Wang H, Liu YB, Ning XJ, Wang QS, Wang FC, Chen D (2017) Oxidation of Ni-based single crystal after grit-blasting during exposure at high temperature. *Mater High Temp* 34(3):215–221. <https://doi.org/10.1080/09603409.2017.1281869>
- [13] Cruchley S, Taylor MP, Ding R et al (2015) Comparison of chromia growth kinetics in a Ni-based superalloy, with and without shot-peening. *Corros Sci* 100:242–252. <https://doi.org/10.1016/j.corsci.2015.07.033>
- [14] Pillai R, Chyrkin A, Galiullin T, Wessel E, Grüner D, Quadackers WJ (2017) External  $\alpha$ -Al<sub>2</sub>O<sub>3</sub> scale on Ni-base alloy 60<sub>2</sub> CA—part II: microstructural evolution. *Corros Sci* 127:27–38. <https://doi.org/10.1016/j.corsci.2017.05.017>

- [15] Li D, Chen J, Etim IP et al (2021) High temperature oxidation behavior of Ni-based superalloy Nimonic95 and the effect of pre-oxidation treatment. *Vacuum* 194:110582. <https://doi.org/10.1016/j.vacuum.2021.110582>
- [16] Hu Y, Cao T, Cheng C et al (2019) Oxidation behavior of a single-crystal Ni-based superalloy over the temperature range of 850 °C–950 °C in air. *Appl Surf Sci* 484:209–218. <https://doi.org/10.1016/j.apsusc.2019.04.089>
- [17] Wang J, Xue H (2021) Wang Y (2021) Oxidation behavior of Ni-based superalloy GH738 in static air between 800 and 1000 °C. *Rare Met* 40(3):616–625. <https://doi.org/10.1007/s12598-020-01513-2>
- [18] Ding Q, Shen Z, Xiang S et al (2015) In-situ environmental TEM study of  $\gamma'$ - $\gamma$  phase transformation induced by oxidation in a nickel-based single crystal superalloy. *J Alloy Compd* 651:255–258. <https://doi.org/10.1016/j.jallcom.2015.07.017>
- [19] Pei H, Wen Z, Zhang Y et al (2017) Oxidation behavior and mechanism of a Ni-based single crystal superalloy with single  $\alpha$ -Al<sub>2</sub>O<sub>3</sub> film at 1000 degrees C. *Appl Surf Sci* 411:124–135. <https://doi.org/10.1016/j.apsusc.2017.03.116>
- [20] Yuan FH, Han EH, Jo CY et al (2003) The effect of crystallographic orientation on the oxidation behavior of a single-crystal nickel-base superalloy. *Oxid Met* 60(3–4):211–224. <https://doi.org/10.1023/A:1026077417712>
- [21] Xu W, Szpunar JA, Zhang L (2015) Effect of surface crystallographic orientation on the oxidation behavior of Ni-based alloy. *Appl Surf Sci* 327:532–536. <https://doi.org/10.1016/j.apsusc.2014.11.126>
- [22] Ma J, Jiang W, Wang J, Zhang Y, Zhang Z (2020) Initial oxidation behavior of a single crystal superalloy during stress at 1100 °C. *Sci Rep* 10(1):3089–3089. <https://doi.org/10.1038/s41598-020-59968-3>
- [23] Schütze M (2016) *Stress effects in high temperature oxidation. Reference module in materials science and materials engineering*, Elsevier, Amsterdam
- [24] Ramsay JD, Evans HE, Child DJ, Taylor MP, Hardy MC (2019) The influence of stress on the oxidation of a Ni-based superalloy. *Corros Sci* 154:277–285. <https://doi.org/10.1016/j.corsci.2019.04.023>
- [25] Ying W, Narita T (2007) Oxidation behavior of the single crystal Ni-based superalloy at 900 °C in air and water vapor. *Surf Coat Technol* 202(1):140–145. <https://doi.org/10.1016/j.surfcoat.2007.05.018>
- [26] Juez-Lorenzo M, Kolarik V, Stamm W, Fietzek H (2012) Oxidation of nickel-based alloys in dry and water vapour containing air. *Mater High Temp* 29(3):229–234. <https://doi.org/10.3184/096034012X13348393336892>
- [27] Oleksak RP, Tylczak JH, Holcomb GR et al (2020) Temperature-dependence of corrosion of Ni-based superalloys in hot CO<sub>2</sub>-rich gases containing SO<sub>2</sub> impurities. *JOM* 72:1822–1829. <https://doi.org/10.1007/s11837-020-04081-z>
- [28] Oleksak RP, Baltrus JP, Nakano J, Nakano A, Holcomb GR, Dogan ON (2017) Mechanistic insights into the oxidation behavior of Ni alloys in high-temperature CO<sub>2</sub>. *Corros Sci* 125:77–86. <https://doi.org/10.1016/j.corsci.2017.06.005>
- [29] Wang L, Jiang WG, Li XW et al (2015) Effect of surface roughness on the oxidation behavior of a directionally solidified Ni-based superalloy at 1,100 °C[J]. *Acta Metall Sinica (English Letters)*. <https://doi.org/10.1007/s40195-015-0211-2>
- [30] Pei H, Wen Z, Li Z, Zhang Y, Yue Z (2018) Influence of surface roughness on the oxidation behavior of a Ni-4.0Cr-5.7Al single crystal superalloy. *Appl Surf Sci* 440:790–803. <https://doi.org/10.1016/j.apsusc.2018.01.226>
- [31] Park SJ, Seo SM, Yoo YS et al (2015) Effects of Al and Ta on the high temperature oxidation of Ni-based superalloys. *Corros Sci* 90:305–312. <https://doi.org/10.1016/j.corsci.2014.10.025>
- [32] Hancock P, Hurst RC (1974) *The mechanical properties and breakdown of surface oxide films at elevated temperatures*. Springer, US
- [33] Pfennig A, Fedelich B (2008) Oxidation of single crystal PWA 1483 at 950 °C in flowing air. *Corros Sci* 50(9):2484–2492. <https://doi.org/10.1016/j.corsci.2008.06.033>
- [34] Hardesty F (1983) An introduction to metallic corrosion. *J Mech Work Technol* 7(3):296–297. [https://doi.org/10.1016/0378-3804\(83\)90007-4](https://doi.org/10.1016/0378-3804(83)90007-4)
- [35] Wagner C (1959) Reaktionstypen bei der Oxydation von Legierungen. *Zeitschrift für Elektrochemie, Berichte der Bunsengesellschaft für physikalische Chemie* 63(7):772–782. <https://doi.org/10.1002/bbpc.19590630713>
- [36] Wagner C (1952) Theoretical analysis of the diffusion processes determining the oxidation rate of alloys. *J Electrochem Soc* 99:369–380. <https://doi.org/10.1149/1.2779605>
- [37] Li J, Peng Y, Zhang J et al (2019) Cyclic oxidation behavior of Ni3Al-based superalloy. *Vacuum* 169(4):108938. <https://doi.org/10.1016/j.vacuum.2019.108938>
- [38] Su YF, Allard LF, Coffey DW et al (2004) Effects of an  $\alpha$ -Al<sub>2</sub>O<sub>3</sub> thin film on the oxidation behavior of a single-crystal Ni-based superalloy. *Metall Mater Trans A* 35(13):1055–1065. <https://doi.org/10.1007/s11661-004-1008-5>
- [39] Birks N, Meier GH, Pettit FS (2006) *Introduction to the high temperature oxidation of metals*. Cambridge University Press, London

- [40] Chapovaloff J, Rouillard F, Wolski K et al (2013) Kinetics and mechanism of reaction between water vapor, carbon monoxide and a chromia-forming nickel base alloy. *Corros Sci* 69:31–42. <https://doi.org/10.1016/j.corsci.2012.09.045>
- [41] Jones DA (1992) Principles and prevention of corrosion. *Mater Des*. <https://doi.org/10.1108/eb007395>

**Publisher's Note** Springer Nature remains neutral with regard to jurisdictional claims in published maps and institutional affiliations.